ARTICLE

Clay Platelet Partition within Polymer Blend Nanocomposite Films by EFTEM

Elisângela M. Linares, Márcia M. Rippel, and Fernando Galembeck*

Institute of Chemistry, University of Campinas, Caixa Postal 6154, 13083-970 Campinas, São Paulo, Brazil

ABSTRACT Transmission electron microscopy (TEM) is the main technique used to investigate the spatial distribution of clay platelets in polymer nanocomposites, but it has not often been successfully used in polymer blend nanocomposites because the high contrast between polymer phases impairs the observation of clay platelets. This work shows that electron spectral imaging in energy-filtered TEM (EFTEM) in the low-energy-loss spectral crossover region allows the observation of platelets on a clear background. Separate polymer domains are discerned by imaging at different energy losses, above and below the crossover energy, revealing the material morphology. Three blends (natural rubber [NR]/poly(styrene−butyl acrylate) [P(S−BA)], P(S−BA)/poly(vinyl chloride) [PVC], and NR/starch) were studied in this work, showing low contrast between the polymer phases in the 40−60 eV range. In the NR/P(S−BA) and P(S−BA)/PVC blend nanocomposites, the clay platelets accumulate in the P(S−BA) phase, while in the P(S−BA)/PVC nanocomposites, clay is also found at the interfaces. In the NR/starch blend, clay concentrates at the interface, but it also penetrates the two polymer phases. These observations reveal that nanostructured soft materials can display complex morphochemical patterns that are discerned thanks to the ability of EFTEM to produce many contrast patterns for the same sample.

KEYWORDS: EFTEM • EELS • electron spectroscopy imaging • polymer blend • latex • clay • nanocomposites

INTRODUCTION

Polymer nanocomposites containing exfoliated clay particles are high-performance materials introduced by the Toyota research group in the early 1990s that attracted great academic and industrial interest. They are currently used in automotive, sports, packaging, health, and other consumer products. This versatility is achieved thanks to the effect of low amounts (typically <10%) of well-distributed clay platelets in polymers, largely improving their mechanical (1−5) and barrier properties (6−9), dimensional stability (10, 11), and fire resistance (12, 13).

Polymer blend nanocomposites have a recognized potential to produce high-performance materials, but the polymer combination should be carefully evaluated because the distribution of clay platelets in the blend may vary because of different interfacial interactions with the blend components. An attractive feature of clay addition to blends is that it improves the compatibility between polymer phases, preventing polymer coalescence during melt processing (14, 15).

The polymer/clay nanocomposites are often characterized by X-ray diffraction (XRD), but this technique does not allow the location of clay layers in one or more polymer phases. For this reason, the investigation of the clay dispersion state and morphology in polymer blends has been probed exclusively by transmission electron microscopy (TEM), providing qualitative and quantitative results (14, 16, 17). This technique requires ultrathin uniform cuts of the sample for viewing the clay within the polymer matrix (16).

Bright-field micrographs obtained by TEM of polymer blend/clay nanocomposites frequently show a high contrast between the polymer phases, which is exacerbated by staining the samples to identify the component polymers. This makes the observation of clay quite difficult, especially in the case of exfoliated, low-contrasting clay platelets (18−26).

Kim et al. (22) describe poly(ethylene oxide) (PEO)/poly(methyl methacrylate) (PMMA) blend nanocomposites and conclude that there is preferential accumulation of organoclay in the PMMA phase. Their conclusion is based only on XRD comparison analysis from homopolymer nanocomposites, because of the difficulty to identify the PMMA and PEO phases in TEM micrographs. Other reports describe similar difficulties (18, 27). The assignment becomes even more difficult when it requires staining (18, 28−30). Sinha Ray and Bousmina (28) describe the presence of the stacks and intercalated organoclay well-dispersed within a polycarbonate/PMMA blend in samples stained with lead (Pb) vapor, but contrast does not allow unequivocal phase identification. Wang et al. (29) used osmium tetroxide staining of the poly(vinyl chloride) (PVC)/nitrile−butadiene rubber (NBR) blend containing clay, but the NBR phase became very dark, avoiding a clear morphology determination.

Energy-filtered transmission electron microscopy (EFTEM) associated with electron energy-loss spectroscopy (EELS) in the high-energy-loss range has been applied to the investigation of the phase separation in polymer blends (32) and interdiffusion of polymers at the interface in laminated films (33). The high-energy-loss region above 100 eV has been invaluable in elucidating polymer particles and film features so that most of the current microchemical and topochemical information on polymers and polymer composites derives from these maps (1, 4, 31, 34−41). It is thus possible to

* To whom correspondence should be addressed. Phone: +55-19-3521-3080. Fax: +55-19-3521-2906. E-mail: fernagal@iqm.unicamp.br.
Received for review August 31, 2010 and accepted November 11, 2010

DOI: 10.1021/am100812m

Published on Web 11/30/2010

associate the spatial distribution of elements with the sample morphology observed in bright-field images. However, the >100 eV spectral energy range has limitations to allow phase distinction of materials that have similar chemical composition, like some polymer blends. It is often necessary to stain the sample in order to visualize the phase array. Staining protocols are often time-consuming, requiring toxic dye manipulation, and they may insert artifacts in the analysis. Furthermore, images acquired in this spectral range expose the sample to intense energy electron beams, causing serious sample damages.

In this work, these limitations are overcome by EFTEM, using molecular mapping techniques based on the low-energy-loss spectral region (31). Spectral differences observed between polymers in the low-energy-loss region are assigned to structural molecular variations that are intrinsic for each polymer and allow distinction of the phases formed by compounds of the same elements. Even slight changes in the molecular structures produce intensity variations in molecular spectra that are, in turn, assessed by using sets of low-energy-loss images that reveal different domains in a polymer blend. Low-loss EELS spectra are more sensitive to variation of the chemical composition in carbon compounds because of their dependence on the molecular electronic structure (42). Energy filters are increasingly available in transmission electron microscopes, and EFTEM imaging requires only low-beam exposure to achieve 1 nm and perhaps higher resolution, without staining. Moreover, contrast between the polymer phases is usually eliminated at some energy loss that appears as a crossover region at the spectra, creating an excellent background for the observation of nonpolymer components, while persisting in other spectral regions. Thus, polymer domain morphology can also be unequivocally obtained on pristine blend samples.

This work presents a novel tool based on EFTEM in the low-energy-loss region for the characterization of three different polymer blends and the respective nanocomposites, revealing clearly the phase distribution and morphology: natural rubber [NR]/poly(styrene−butyl acrylate) [P(S−BA)], P(S−BA)/PVC, and NR/starch. Two blends are made using NR and starch obtained from natural resources, which makes them attractive as "green" materials, while the styrene−acrylic/PVC blend is a plasticized PVC material but exempt from unsafe plasticizers. These polymers are representative of different polymer types to warrant that the present results are not limited only to one or another polymer class.

EXPERIMENTAL SECTION

Materials. Natural rubber [NR] latex was supplied by Talismã (Mirassol, Brazil). Poly(styrene−butyl acrylate) [P(S−BA)] was Acronal 295 D latex supplied by BASF (São Paulo, Brazil), and poly(vinyl chloride) [PVC] was Norvic L66GA latex from Braskem (Maceió, Brazil). Sodium montmorillonite (Na-Cloisite) was acquired from Southern Clay Products (Gonzales, TX). Anionic cassava starch was Agetex 90 supplied by Inpal (Rio de Janeiro, Brazil). These materials were used as received.

Blend and Nanocomposite Preparation. NR/P(S−BA) and P(S−BA)/PVC blends were prepared with a solid weight ratio of 7:3. Suitable amounts of lattices were mixed at room temperature, diluted to 30 wt % of solids content, and stirred for 30 min. The dispersions were cast within a mold and then dried at 60 °C for at least 24 h. The nanocomposite containing 5 phr (per hundred resin) clay was prepared by adding an aqueous 2 wt % clay dispersion to the lattices. The resulting dispersions were diluted to 20 wt % solids, cast, and dried at 60 °C.

An NR/starch blend nanocomposite containing 6 phr clay was prepared as described above but using a starch/clay dispersion prepared with ca. 5 wt % solids in distilled water and heated to 70 °C under mechanical stirring. After starch gelatinization began, the starch/clay dispersion was heated for 20 min, and then it was added to the NR latex at room temperature and mechanically stirred for 5 min. The final dispersion was filtered for air bubble removal and dried in a casting mold at 50 °C for 24 h.

Ultramicrotomy. Ultrathin (ca. 60 nm) sections for TEM analysis were cut with a diamond knife (Drukker) using a Leica EM FC6 cryoultramicrotome. The blend and nanocomposite films were cut at −150 °C, cooling with liquid dinitrogen. A drop of supersaturated sucrose was used to collect the thin cuts and to transfer them to the microscope grids. These were then left floating in deionized water within a beaker for 5−10 min to wash out sucrose, followed by drying at room temperature.

Electron Microscopy. Images were acquired using a Carl Zeiss CEM-902 transmission electron microscope equipped with a Castaing−Henry−Ottensmeyer filter spectrometer, operating at 80 kV. EELS spectra were acquired in the 0−90 eV range from the desired sample areas. EFTEM was used to obtain images in the 25−90 eV loss range, using a 7 eV energy slit. The images were recorded using a Proscan high-speed, slow-scan CCD camera and digitized (1024−1024 pixels, 8 bits) in the iTEM Universal TEM Imaging Platform.

RESULTS AND DISCUSSION

Figure 1 shows a set of bright-field and low-loss EFTEM images taken from a thin cut of the NR/P(S−BA) blend and EELS spectra of NR and P(S−BA) polymers. The bright-field image shows distinctly brighter domains of one phase dispersed through a darker matrix.

EFTEM images show contrast inversion around 50 eV, due to EELS spectra of the isolated polymers crossing in this energy-loss range. Even though spectra are qualitatively similar, their quantitative differences allow identification of the two polymer phases: P(S−BA) domains are brighter at energy losses lower than 50 eV (including bright-field images), and NR domains are dark, but they become brighter in the 50−90 eV loss range. The image acquired at 90 eV energy loss shows contrast within the P(S−BA) particles and also along the matrix. Rubber is mostly coalesced, but discrete rubber particles are also seen, as indicated by arrows in Figure 1.

To understand the differences between the spectra of different polymers, we recall that the spectrum of molecular compounds is dominated by Rydberg transitions and ionization potentials (first and higher) added to well-known outer-shell (L, M) electron excitations. Spectra change depending on the molecular electronic structure and thus on the overall bonding structure. C−C and C−H bonds dominate the polymer elemental composition, but NR also contains nitrogen, phosphorus, sulfur, calcium, potassium, and sodium, besides carbon, hydrogen, and oxygen. This introduces additional contributions from their outer electron transitions

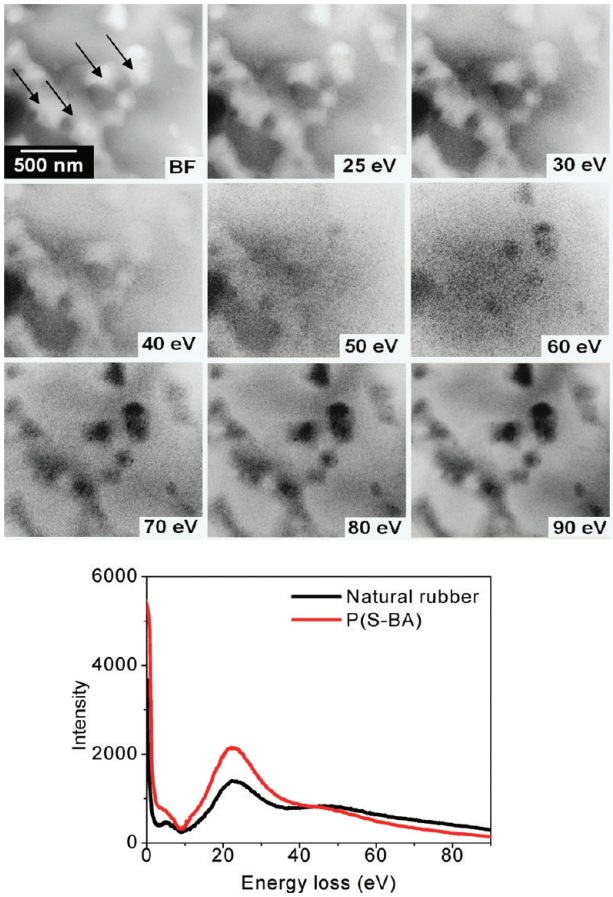

FIGURE 1. (Top left) Bright-field and low-loss EFTEM images (25−90 eV energy loss) of a thin cut from a NR/P(S−BA) blend with a weight ratio of 7:3. EELS spectra of NR and P(S−BA). Rubber particles are indicated by arrows.

to the low-energy-loss spectra. Multiple scattering further complicates this. Therefore, spectral differences after 50 eV are due to the following factors: density, contributions from the higher ionization potentials of bonding electrons, contributions from the outer electrons from noncarbon elements, and molecular orbital energy patterns for the molecules involved. This is why these spectra are sensitive fingerprints for polymer composition, even if they have few pronounced features.

In Figure 2, a bright-field image and an EFTEM series of images of the NR/P(S−BA) blend nanocomposite show important morphological and structural differences with the pure polymer blend. Silicate platelets are well dispersed in the film, but a bright-field image does not allow identification of polymer domains containing platelets. Images in the contrast inversion region, ca. 40−50 eV, show that clay platelets are oriented parallel to the film surface. Moreover, clay distribution is not uniform, and they accumulate in the domains appearing darker in the 50−90 eV loss images, made out of P(S−BA). Besides exfoliated clay platelets, aggregates with a few tens of nanometers can be seen.

The P(S−BA) dispersed domain shape in the nanocomposite is different from that of the original polymer blend. P(S−BA) domains are well-separated, and their aspect ratio is close to unity in the blend but they form noncoalesced

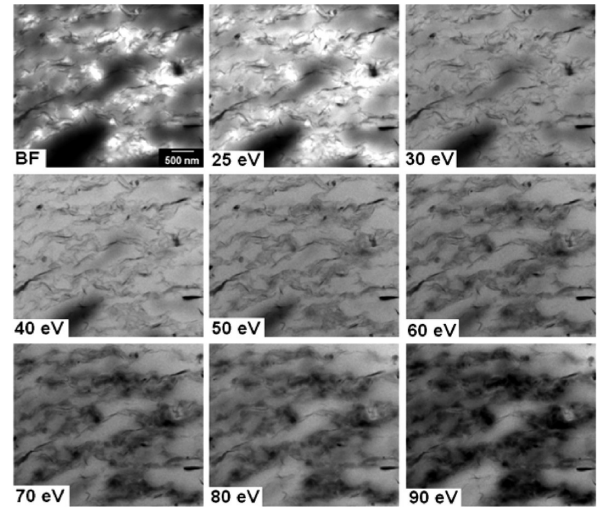

FIGURE 2. (Top left) Bright-field and low-loss EFTEM (25−90 eV energy loss) images of a thin cut from the clay nanocomposite of a NR/P(S−BA) blend with a weight ratio of 7:3.

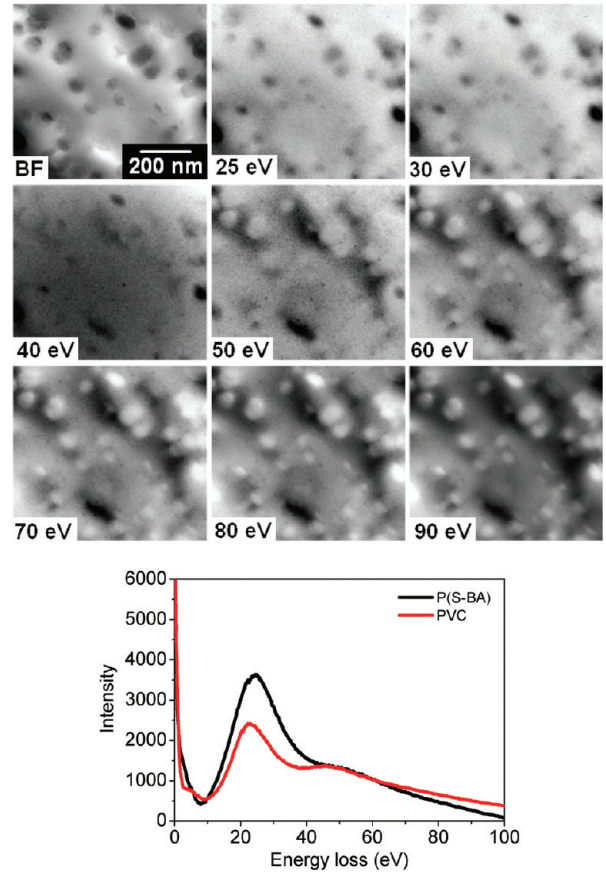

FIGURE 3. Low-loss EFTEM images (25−90 eV energy loss) and EELS spectra from a thin cut of a P(S−BA)/PVC blend with a weight ratio of 7:3.

aggregates containing clay with a 2−5 aspect ratio, in the nanocomposite.

A P(S−BA)/PVC blend was also analyzed by EFTEM as an example of a blend formed by very different polymers, and an image series is shown in Figure 3. The bright-field image shows spherical PVC particles well dispersed in the P(S−BA) matrix, as expected considering that the blend film was dried at 60 °C, below the PVC glass transition temperature

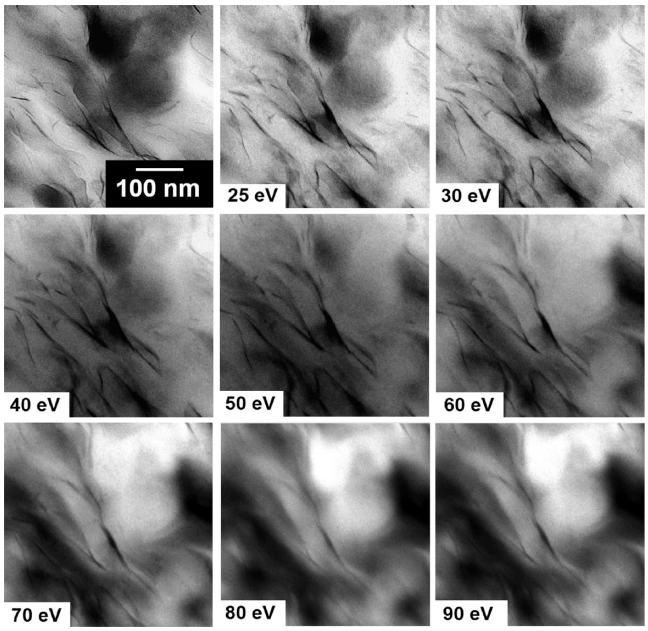

FIGURE 4. (Top left) Bright-field and low-loss EFTEM (25−90 eV energy loss) images of a thin cut from the clay nanocomposite of P(S−BA)/PVC with a weight ratio of 7:3.

($T_{g,PVC}$ = 85 °C). In the low-loss EFTEM image series, PVC particles are darker below 40−50 eV loss but they are brighter at higher energy loss. PVC particles show contrast variations, which means that their chemical composition is not uniform (1, 35−41, 43, 44).

In the nanocomposite micrographs shown in Figure 4, the clay platelets appear well-exfoliated in the P(S−BA) matrix and some are also located at the P(S−BA)/PVC interface. The images at 80−90 eV loss are especially convenient to observe this because PVC domains appear very bright.

Blends of rubber and starch form soft films that block the microtome knife even at −140 °C, preventing the formation of smooth cuts that can be viewed in the microscope. However, blend/clay nanocomposite films are also soft, but they resist handling very well, yielding high-quality ultramicrotome cuts. Figure 5 shows a bright-field image and a series of EFTEM images of a NR/starch/clay nanocomposite, which is an example of a very complex system formed by natural raw materials. The starch domains appear bright in the images (including the bright-field ones) below 50 eV loss because this polymer shows a higher spectral intensity than NR, as seen in the energy-loss spectrum in Figure 5. The images show two coalesced phases with good interfacial adhesion. Most clay platelets are located at the interface, but they also penetrate in the polymer phases, as seen in the image acquired at 50 eV.

Clay platelet number distributions within polymer domains were measured using the Image-Pro Plus software, and the results are presented in Table 1. In P(S−BA)/NR and P(S−BA)/PVC blend nanocomposites, clay platelets accumulate in the P(S−BA) domains and lower amounts are found at the interfaces. In a NR/starch blend nanocomposite, most platelets (51 %) are found at the interfaces, followed by 32 % in the starch and 16 % in the NR domains.

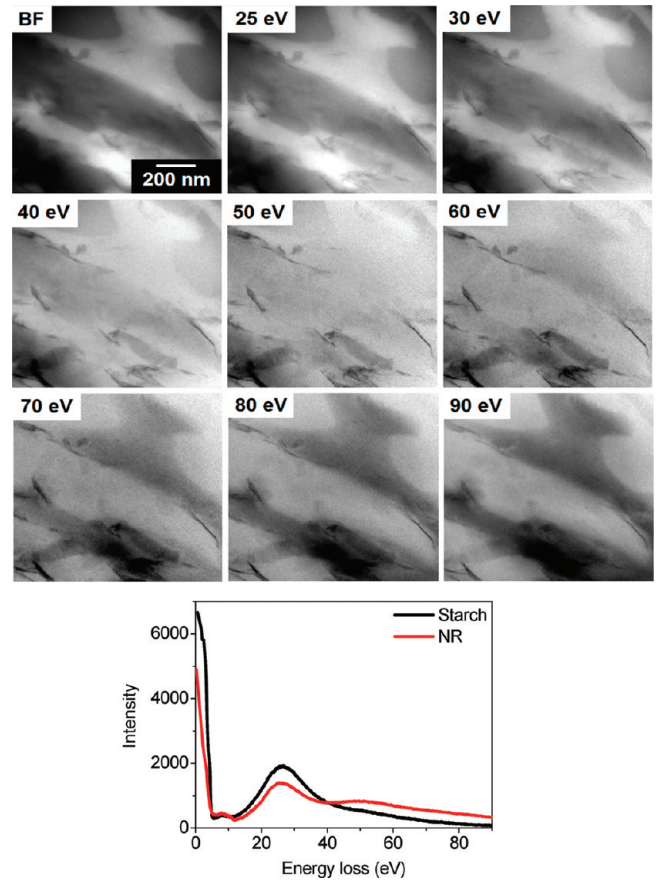

FIGURE 5. (Top left) Bright-field and low-loss EFTEM (25−90 eV energy loss) images of a thin cut from the nanocomposite of the NR/starch blend with a weight ratio of 7:3. EELS spectra of NR and starch.

Table 1. Clay Platelet Numbers Counted on Polymer Domains and Interfaces in the Presented Images[a]

blend	P(S−BA)	NR	starch	PVC	interface
P(S−BA)/NR	78 (52 %)	30 (20 %)			41 (28 %)
P(S−BA)/PVC	44 (90 %)			0	5 (10 %)
NR/starch		6 (16 %)	12 (32 %)		19 (51 %)

[a] The corresponding percentages are given in parentheses.

The molecular mapping technique used in this work provides detailed information on the spatial distribution of the three component phases of blend nanocomposites—two polymers and clay—showing clearly how the minor clay component is partitioned among the polymer phases and interfaces. This is done on as-cut samples, and staining is completely unnecessary. Exfoliated clay platelets are identified on a chemically complex matrix due to low contrast between the polymer phases in the spectral crossover region; thus, it is essential to have at least some images with low contrast between the polymer phases.

Imaging above and below the crossover energy loss allows unequivocal polymer phase identification and assessment of morphology as well as chemical composition uniformity of both coalesced and particulate polymer domains, independent of the presence of clay particles.

In the two blend nanocomposites made with a styrene−acrylic latex, individual clay platelets together with a few tactoids are found most often in the styrene−acrylic domains, while NR or PVC domains contain very few clay particles. Clay particles in the NR/starch blend are accumulated at the interfaces but penetrating the polymer phases, to a limited extent.

In two systems, clay particles show a strong affinity for the styrene−acrylic polymer. Thus, clay platelets are not simply trapped between latex particles during latex−clay dispersion drying. Rather, this strongly suggests that clay segregation in one or another type of domain takes place at an earlier stage during nanocomposite formation, when mass transfer within the drying dispersion is still fast, probably due to colloidal phase separation (45).

The difference in the polymer domain shapes in the polymer-only blends and the blend nanocomposites suggests that either the cohesive energy of the polymer domains filled with clay increases, compared to the polymer blends, or the interfacial energy between the two polymer phases decreases, or both. Clay contribution to increase cohesion in latex nanocomposites was previously demonstrated (1).

Three different polymer pairs were analyzed, showing that the present strategy can be easily extended to many different polymer systems, even containing similar or variable compositions such as NR and starch.

The wealth of observations done in this work has not been previously attained in comparable complex systems, and it cannot be matched by any other current technique. Scanning transmission X-ray microscopy (STXM) and TEM have also been used to map polymers and clay (46). STXM yields molecular maps of the polymer domains in a blend, and these are correlated to the bright-field images obtained with TEM, thus avoiding staining. STXM images are taken at specific energies of absorption of one of the polymers, yielding compositional (molecular) maps, and the phase assignment is used to interpret the TEM micrographs. Although STXM is effective in identifying the polymer phases, it cannot image the finer clay particles because if its low resolution (ca. 40 nm).

There are many possibilities for extending the present results for samples as thick as some hundreds of nanometers, as shown in previous work (47, 48). Moreover, the procedures used in this work can be used with colloidal particles of any type, chemical composition, and size, from a few nanometers to a few micrometers, and there is no restriction to the examination of systems with higher numbers of particle constituents, both polymer or mineral.

CONCLUSIONS

The distribution of three components of nanocomposite polymer blends is observed quantitatively with high spatial resolution using molecular mapping based on EFTEM at low electron energy loss. Cancellation of the contrast among polymer phases at 40−50 eV loss allows the observation of clay nanoparticle orientation and spatial distribution in the polymer blend. Clay platelets locate preferentially within the styrene−acrylic resin in two blends [NR/P(S−BA) and PVC/P(S−BA)], but they accumulate at the interface, in NR/starch blends. Polymer phase identification is also done unequivocally, acquiring EFTEM images in other energy ranges (<40 or >50 eV). These results demonstrate the ability of EFTEM molecular mapping to identify components of complex nanostructured systems, suggesting that it can be extended to many other multicomponent systems including those containing phases with different molecular composition but formed by the same elements.

Acknowledgment. E.M.L. is thankful for a fellowship from Fapesp. This is a contribution from the Petrobras Nanotechnology Thematic Network and INCT Program (MCT and Fapesp), through Inomat (National Institute for Complex Functional Materials).

REFERENCES AND NOTES

(1) Bragança, F. D.; Valadares, L. F.; Leite, C. A. D.; Galembeck, F. *Chem. Mater.* **2007**, *19*, 3334–3342.
(2) Valadares, L. F.; Linares, E. M.; Bragança, F. C.; Galembeck, F. *J. Phys. Chem. C* **2008**, *112*, 8534–8544.
(3) Fornes, T. D.; Yoon, P. J.; Keskkula, H.; Paul, D. R. *Polymer* **2001**, *42*, 9929–9940.
(4) Valadares, L. F.; Leite, C. A. P.; Galembeck, F. *Polymer* **2006**, *47*, 672–678.
(5) Xu, Y. J.; Brittain, W. J.; Vaia, R. A.; Price, G. *Polymer* **2006**, *47*, 4564–4570.
(6) Bhole, Y. S.; Wanjale, S. D.; Kharul, U. K.; Jog, J. P. *J. Membr. Sci.* **2007**, *306*, 277–286.
(7) Brody, A. L. *Food Technol.* **2007**, *61*, 80–83.
(8) Xu, B.; Zheng, Q.; Song, Y. H.; Shangguan, Y. *Polymer* **2006**, *47*, 2904–2910.
(9) Kint, D. P. R.; Seeley, G.; Gio-Batta, M.; Burgess, A. N. *J. Macromol. Sci., Part B: Phys.* **2005**, *B44*, 1021–1040.
(10) Ding, Y. Y.; Gui, Z.; Zhu, E.; Wang, Z. Z.; Hu, Y.; Song, L. *J. Mater. Res.* **2007**, *22*, 3316–3323.
(11) Hossain, M. D.; Kim, W. S.; Hwang, H. S.; Lim, K. T. *J. Colloid Interface Sci.* **2009**, *336*, 443–448.
(12) Morgan, A. B.; Chu, L. L.; Harris, J. D. *Fire Mater.* **2005**, *29*, 213–229.
(13) Pack, S.; Si, M.; Koo, J.; Sokolov, J. C.; Koga, T.; Kashiwagi, T.; Rafailovich, M. H. *Polym. Degrad. Stab.* **2009**, *94*, 306–326.
(14) Wang, Y.; Zhang, Q.; Fu, Q. *Macromol. Rapid Commun.* **2003**, *24*, 231–235.
(15) Paul, D. R.; Robeson, L. M. *Polymer* **2008**, *49*, 3187–3204.
(16) Pavlidou, S.; Papaspyrides, C. D. *Prog. Polym. Sci.* **2008**, *33*, 1119–1198.
(17) Ray, S. S.; Okamoto, M. *Prog. Polym. Sci.* **2003**, *28*, 1539–1641.
(18) Martins, C. G.; Larocca, N. M.; Paul, D. R.; Pessan, L. A. *Polymer* **2009**, *50*, 1743–1754.
(19) Zhu, Y.; Xu, Y.; Tong, L.; Xu, Z.; Zhengping, F. *J. Appl. Polym. Sci.* **2008**, *110*, 3130–3139.
(20) Khatua, B. B.; Lee, D. J.; Kim, H. Y.; Kim, J. K. *Macromolecules* **2004**, *37*, 2454–2459.
(21) Voulgaris, D.; Petridis, D. *Polymer* **2002**, *43*, 2213–2218.
(22) Kim, H. B.; Choi, J. S.; Lee, C. H.; Lim, S. T.; Jhon, M. S.; Choi, H. J. *Eur. Polym. J.* **2005**, *41*, 679–685.
(23) Lee, M. H.; Dan, C. H.; Kim, J. H.; Cha, J.; Kim, S.; Hwang, Y.; Lee, C. H. *Polymer* **2006**, *47*, 4359–4369.
(24) González, I.; Eguiazábal, J. I.; Nazábal, J. *Eur. Polym. J.* **2006**, *42*, 2905–2913.
(25) Mondragón, M.; Hernández, E. M.; Rivera-Armenta, J. L.; Rodríguez-González, F. J. *Carbohydr. Polym.* **2009**, *77*, 80–86.
(26) Vo, L. T.; Giannelis, E. P. *Macromolecules* **2007**, *40*, 8271–8276.
(27) Varghese, S.; Gatos, K. G.; Apostolov, A. A.; Karger-Kocsis, J. *J. Appl. Polym. Sci.* **2004**, *92*, 543–551.
(28) Ray, S. S.; Bousmina, M. *Macromol. Rapid Commun.* **2005**, *26*, 450–455.
(29) Wang, Q.; Zhang, X.; Jin, Y.; Gui, H.; Dong, W.; Lai, J.; Liu, Y.; Gao, J.; Huang, F.; Song, Z.; Qiao, J. *Macromol. Mater. Eng.* **2006**, *291*, 655–660.

(30) Kontopoulou, M.; Liu, Y.; Austin, J. R.; Parent, J. S. *Polymer* **2007**, *48*, 4520–4528.
(31) Linares, E. M.; Valadares, L. F.; Silva, C. A.; Rezende, C.; Leite, C. A. P.; Galembeck, F. *Anal. Chem.* **2009**, *81*, 2317–2324.
(32) Liao, Y.; Horiuchi, S.; Nunoshige, J.; Akahoshi, H.; Ueda, M. *Polymer* **2007**, *48*, 3749–3758.
(33) Liao, Y.; Nakagawa, A.; Horiuchi, S. *Macromolecules* **2007**, *40*, 7966–7972.
(34) Silva, C. A.; Galembeck, F. *Colloids Surf., A* **2010**, *363*, 146–154.
(35) Costa, C. A. R.; Leite, C. A. P.; Galembeck, F. *Langmuir* **2006**, *22*, 7159–7166.
(36) Rippel, M. M.; Leite, C. A. P.; Lee, L.-T.; Galembeck, F. *J. Colloid Interface Sci.* **2005**, *288*, 449–456.
(37) Rippel, M. M.; Leite, C. A. P.; Lee, L.-T.; Galembeck, F. *J. Colloid Polym. Sci.* **2005**, *283*, 570–574.
(38) Rippel, M. M.; Lee, L.-T.; Leite, C. A. P.; Galembeck, F. *J. Colloid Interface Sci.* **2003**, *268*, 330–340.
(39) Braga, M.; Leite, C. A. P.; Galembeck, F. *Langmuir* **2003**, *19*, 7580–7586.
(40) Costa, C. A. R.; Leite, C. A. P.; Galembeck, F. *J. Phys. Chem. B* **2003**, *107*, 4747–4755.
(41) Rippel, M. M.; Leite, C. A. P.; Galembeck, F. *Anal. Chem.* **2002**, *74*, 2541–2546.
(42) Yakolev, S.; Libera, M. *Micron* **2008**, *39*, 734–740.
(43) Amalvy, J. I.; Asua, J. M.; Leite, C. A. P.; Galembeck, F. *Polymer* **2001**, *42*, 2479–2489.
(44) Stubbs, J. M.; Sundberg, D. C. *Polymer* **2005**, *46*, 1125–1138.
(45) Chan, D. Y. C.; Linse, P.; Petris, S. N. *Langmuir* **2001**, *17*, 4202–4210.
(46) Si, M.; Araki, T.; Ade, H.; Kilcoyne, A. L. D.; Fisher, R.; Sokolov, J. C.; Rafailovich, M. H. *Macromolecules* **2006**, *39*, 4793–4801.
(47) Valadares, L. F.; Bragança, F. C.; Silva, C. A.; Leite, C. A. P.; Galembeck, F. *J. Colloid Interface Sci.* **2007**, *309*, 140–148.
(48) Kortje, K. H.; Paulus, U.; Ibsch, M.; Rahmann, H. *J. Microsc.* **1996**, *183*, 89–101.

AM100812M